ARTICLE

Check for updates

Slab-derived fluid storage in the crust elucidated by earthquake swarm

Yusuke Mukuhira[1✉], Masaoki Uno [2] & Keisuke Yoshida [3]

Slab-derived fluids control crustal dynamics in the subduction zone. However, the slab-derived fluid budget has never been quantified beyond a geophysical and geological spatiotemporal resolution. Here, we target an intense earthquake swarm associated with the M9 Tohoku earthquake, which represented the critical dynamic behavior of slab-derived fluid. The fluid volume involved has been quantified, with a plausible range of $10^6-10^8\,m^3$, by utilizing injection-induced seismicity insights. Comparisons with geological proxies suggest that the estimated fluid volume can be accumulated via supply from the lower crust within $10^2–10^4\,y$. Our study demonstrated such amount of aqueous fluid stored at the midcrustal level, which triggered consecutive swarm activity for ~2 y with the Tohoku earthquake, suggesting a possible link between earthquake swarms to M9 class earthquakes (10^3 y cycle) and mineral veins and deposits. This study has shed light on the quantitative understanding of the dynamic slab-derived fluid budget.

---

[1] Institute of Fluid Science, Tohoku University, Sendai, Japan. [2] Graduate School of Environmental Studies, Tohoku University, Sendai, Japan. [3] Research Center for Prediction of Earthquakes and Volcanic Eruptions, Tohoku University, Sendai, Japan. ✉email: mukuhira@tohoku.ac.jp

Crustal fluids are critical for energy and material transfer (e.g., ore deposits) from the Earth's interior towards its surface, and the dynamic behavior of the crust (e.g., crustal deformation, earthquakes, and volcanic activity)[1–6]. The main source of crustal fluids is aqueous fluids released by the slab dehydration at subduction zones[1,2,7–10]. The migration of these fluids in the overlying mantle and crust controls the long-term stability of the ocean, generation of arc magmas, and earthquakes (both at plate margins and within the plate)[1,2,8,10]. The aqueous fluid-bearing areas in the crust are generally demarcated as high-conductivity regions by magnetotelluric measurements[6,9], and/or low-velocity zones by seismic tomographies[3,10]. These areas are frequently located beneath the seismogenic zones of the arc crust[3,6,9]. Quartz veins in exhumed crustal materials also suggest highly channelized flow paths in the crust. Traces of repeated fracturing in the crack-seal veins support that aqueous fluids accumulate in the crust; thereby, raising the fluid pressure to near lithostatic pressure, and activate fractures in the rocks. Subsequently, the fluid flows until its pressure drops, and/or the newly formed fracture is entirely sealed by quartz precipitation[5,11,12]. Such fault-valve behavior may control the recurrence of tremors and earthquakes at the plate margin and within the plate[4,13], which may be linked to hazardous earthquakes. Fluid storage in the crust and their subsequent release during earthquakes are further supported by the migration of hypocenters during earthquake swarms[14,15], which are sometimes accompanied by the eruptions of fluids[16]. Elemental transport by fluid flow along the crustal faults and under volcanoes generates epithermal–mesothermal gold[5,17] and porphyry copper deposits[18,19], which are geological manifestations of episodic fluid flow in the lower crust[5,20]. Fluid volume and flux govern the dynamic and static behaviors of the various geological processes. Geophysical studies have revealed the macroscopic distribution of fluid in the subduction zone[3], while geochemical studies have estimated long-term fluid flux from subducting plates[1,2,7] and volcanoes, solidifying magmatic chambers and dikes[8,21–23]. However, the absolute amounts and flow rates of the crustal fluids are highly uncertain, owing to the limited resolution of those approaches in the lower crust. Such deep crust fluids principally originate from the dehydration of the subducting slab[1,7]. Hydrous magmas generated in the subarc mantle carry aqueous fluids that are released into the lower and middle crust[8]. These fluids then migrate to the bottom of the upper crust and deep geothermal reservoirs[3,10,22,24].

However, dehydration of the subducting slab and release of fluids from hydrous magmas is a slow process, governed by the velocity of the subducting slab and cooling of a pluton, respectively, and there is a huge time gap between the Ma-scale geological fluid flux and the seismogenic fluid flux, the duration of which ranges from seconds to years. Thus, there has been no means of knowing the dynamic behavior of slab-derived fluids beyond the geologic spatiotemporal time resolution, though it could connect intense seismogenic activities.

The 2011 M9 Tohoku earthquake in Japan triggered numerous swarms[14,15,25] and provided a unique opportunity to directly constrain the crustal fluid volume using seismological data. Integrating the insights from a recent and detailed study of the injection-induced seismicity fields[26–28] with those of the swarm observations, we present the first estimate of the fluid volume stored in the crust before the M9 Tohoku earthquake. Critical comparisons with background geologic fluid flux revealed the episodic nature of fluid storage and release in the arc crust within a period of 10^2–10^4 y.

Results and discussion
Earthquake swarm associated with the M9 Tohoku earthquake.
Earthquake swarm in the crust is a sequence of earthquakes without a clear mainshock, and thought to be a natural version of injection-induced seismicity. They typically show clear spatial migration over time and are interpreted to be caused by fluid migration[18,19,26]. For instance, the slab-derived fluids were the probable cause of the earthquake swarm near the Yamagata–Fukushima border in Japan[14,15] (Fig. 1a). This earthquake swarm activated approximately a week after the 2011 M9 Tohoku earthquake, which had occurred hundreds of kilometers away, even though the strain energy was reduced by the Tohoku earthquake[14]. The activation of this swarm can be attributed to the increase in pore pressure due to upward fluid migration following the Tohoku earthquake[14] (Fig. 1b). A low-velocity region[10] and a paleo-caldera were found to exist just below and above the swarm region, respectively, suggesting the existence of an upward path for fluids. Indeed, during the swarm activity, the earthquake hypocenters moved from deep to shallow levels through multiple faults[14] (Fig. 1c). Additionally, various features of seismic activity were similar to those of injection-induced seismicity[14,29]. After the Tohoku earthquake, similar earthquake swarms occurred in various parts of eastern Japan[15], but the one near the Yamagata–Fukushima border was the largest.

Estimation of fluid volume. We employed two representative models for the injection-induced seismicity studies to connect seismic activity and causal fluid volume. The cumulative seismic moment of the swarm was used to estimate the fluid volume using McGarr's model[27] (see "Methods"). The estimated fluid volume that led to the swarm activation was 8.0×10^5 m^3. We also utilized the seismogenic index (SI) model based on pore pressure diffusion[28] (see "Methods"). We estimated the fluid volume (Supplementary Figs. 3 and 4) with previously observed SI sets (ranging from -2.0 to 1.0)[28,30] from geothermal reservoirs in crystalline rocks. The estimated fluid volume is in the order of 0.082–82×10^6 m^3.

In addition to injection-induced seismicity, hydrological models were also adopted to estimate the fluid volume that caused the earthquake swarm. We modeled the spatiotemporal migration of the swarm as a proxy for fluid flow using Darcy's law or the cubic law (see Methods). This law allows the estimation of the flow rate and its time integral, i.e., the fluid volume when the flow zone and hydraulic parameters (diffusivity or permeability) are available. We modeled the flow zone and diffusivity from the time-series migration of the hypocenters[31]. The resultant fluid volume estimated using Darcy's law ranged from approximately 5.1×10^6–1.4×10^8 m^3, while that using the cubic law was approximately 2.8×10^5–7.6×10^6 m^3 for the pressure difference ($\Delta P = 10$–270 MPa) (Supplementary Figs. 6–15).

In summary, the possible range of fluid volume estimated using four different methods was in the order of 10^5–10^8 m^3 (Supplementary Fig. 16). All the models suggest that a large portion of the fluid was released in the early part of the swarm sequence (Supplementary Figs. 2, 3, 5, 14, and 15), which coincides with the very intense early seismic swarm activity[14]. The fluid volume estimated for each cluster (Supplementary Figs. 2, 3, 5, 14, and 15), indicated differences among the clustered swarms depending on the scale and amount of seismic activity. All four models were based on different physical processes, and this multidisciplinary approach was utilized to evaluate the values that denote the dynamics of slab-derived fluids in swarm sequences.

Considering the methodology, the estimate from McGarr's model can be denoted as the lower limit of the fluid volume[27] and is nearly the same value of lower limit of the SI model with the representative value of SI $= 0.5$ (Basel, EGS field). Therefore, we can constrain the lower bound of fluid volume as 10^6 m^3. The SI
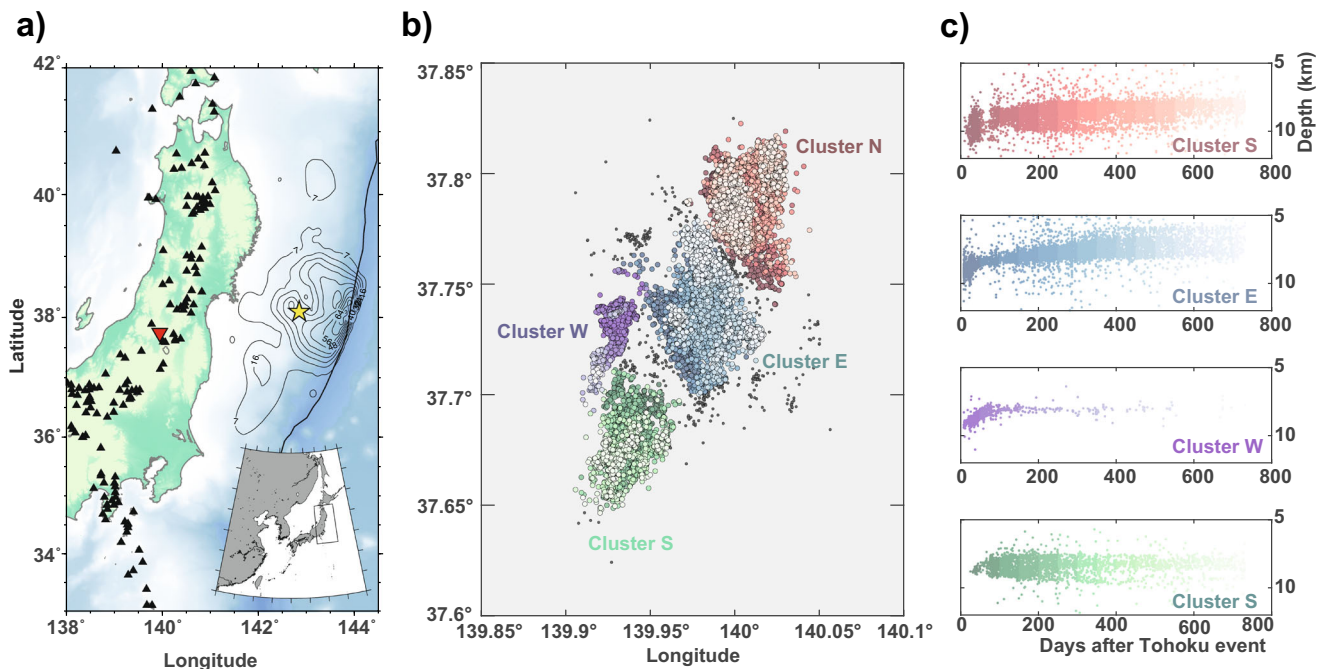
Fig. 1 Field overview including location and seismic activity. a Study area (red triangle) in the Japan volcanic arc. Black triangles represent the Quaternary volcanoes. The star marks the epicenter of the Tohoku earthquake, and its slip distribution is also shown. **b** Hypocenter distribution of the swarm near the Yamagata-Fukushima border[12]. The swarm has been classified into four clusters[12], shown with different color schemes and their respective occurrence times. **c** Cross-sectional time migration patterns of the swarm hypocenters for each cluster.

model presented the widest range of fluid volume up to $10^8 \, m^3$, for the lowest SI value −2 (Soultz, EGS field)[28,30]. Darcy's law also estimated as a large fluid volume, similar to that of the SI model. One well reasoned estimate of $\Delta P = 140 \, MPa$ (pore pressure at source: lithostatic, pore pressure at the edge of swarm region: hydrostatic) presented a similar value to the upper bound of the SI model. Consequently, fluid volume estimates from four different models fall in the range of two orders; 10^6–$10^8 \, m^3$, considering the overlapped values of well reasoned cases from each method (Fig. 2). The upper range of fluid volume might be overestimated. The seismo-tectonic activity level (SI value) of our study area in the mobile belt is unlikely to be the same as that in Europe, such as −2 (Soultz, EGS field)[28,30], which led to the upper limit of fluid volume estimation. In addition, very intense swarm activity in the first 50 days makes it difficult to estimate the reasonable apparent diffusivity or permeability in that period. Possible overestimation in SI model and in Darcy's law might be present in higher fluid volume estimates. Indeed, we defined this order range of the fluid volume (10^6–$10^8 \, m^3$) as the plausible range and explicate following multidisciplinary discussions based on this range.

It is surprising that such an amount of free aqueous fluid exists beneath the swarm region of the mid-crustal level since the apertures (cracks/pores/openings) in the grain boundary are extremely small ($\sim 10^{-9} \, m$)[32]. The maximum length of mechanically stable cracks in granite under crustal condition had been estimated as <20 m[33], where their aspect ratios would be $<10^{-2}$–10^{-3}[34], showing that a voluminous body of water is mechanically unstable in the deep crust. However, other geological evidence, such as mineral veins and mineral deposits, support past massive fluid flows.

As the amount of fluids in the crust has been discussed for different timescales ranging from years to millions of years[5,8,17,20,21,23], this finding would promote a comprehensive understanding in the field of slab-derived fluids, while simultaneously achieving a breakthrough in the geological calculations of

fluid budgets since they have not previously been quantified to understand their dynamic behavior.

Duration of fluid storage. The constrained fluid volume (10^6–$10^8 \, m^3$) allows us to evaluate the duration of fluid storage in the crust prior to the swarm. The upward movement of the swarm (Fig. 1c) strongly suggests that the fluids were supplied from the deeper crust and were stored near the swarm zone. The swarm is located near the Bandai-Azuma-Adatara volcanic clusters[35] below the Miocene Otoge volcanic caldera[36] (Fig. 3a). The uppermost mantle and the lower crust are characterized by low Vs and high Vp/Vs ratio[10,37] indicating the presence of melt or partial melting zones (Supplementary Fig. 1 and Fig. 3a)[38]. These volcanic clusters were supplied with highly hydrous magma (H_2O = ~5 wt.%)[21,39,40], which would release a large amount of H_2O during solidification in the lower and/or upper crust[22]. In the NE Japan arc, many seismic reflectors exist beneath volcanic regions in the upper crust (<18 km), suggesting the existence of aqueous fluids in the planar fractures or cracks[41,42]. Therefore, we suggest that the fluids supplied to the base of the swarm originated from the partial melting zones in the lower crust and were stored in the upper crust within fractures or cracks (Fig. 3a).

The background H_2O flux under the NE Japan arc is predominantly supplied from hydrous melt (~13 t/yr/m of the arc length)[8], consistent with the H_2O fluxes observed in the upper crustal fossil magma chambers (4–17 t/yr/m)[21,39], which corresponds to an average H_2O flux of 10^{-4}–$10^{-3} \, m^3/m^2/yr$. Assuming the area of the swarm region to be $10 \times 10 \, km^2$, the estimated fluid volume (10^6–$10^8 \, m^3$) corresponds to the accumulation of fluids over 10–10^4 years (Fig. 3b). These fluid accumulation periods are much longer than the interval between the Tohoku earthquake and the beginning of the swarm (~7 days), suggesting that fluids had been stored in the crust prior to the Tohoku earthquake in the form of mobile fluid. Additionally, the Japan Meteorological Agency (JMA) catalog (since 1919) and
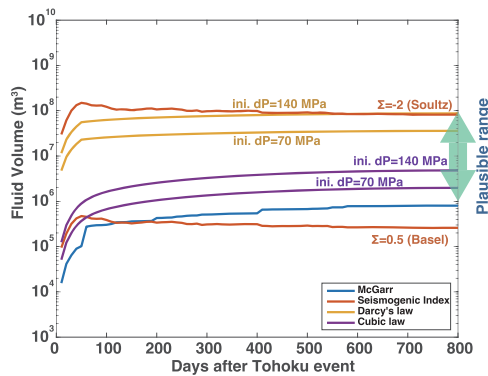
Fig. 2 Fluid volume estimation. Each line corresponds to the well-reasoned upper and lower case for each model. Vertical arrows indicate the plausible range of fluid volume estimation (green) and all possible range of that (gray).

modern seismic records from the 1970s do not suggest any seismic activity in this region. Thus, the accumulation periods have been longer than ~90 y and possibly ranged from hundreds to tens of thousands of years. This range included the last M9 Jogan earthquake (869 AD) at least, suggesting the possibility that such seismic swarms occur periodically accompanying the M9 class earthquakes.

A total of 10^6–10^8 m^3 of fluids sourced from the lower crustal partial melting zones were accumulated beneath the swarm region within 10^2–10^4 y, thereby increasing the pore pressure. However, the flow pathway connecting it to the swarm region was sealed by the fault-valve behavior. The Tohoku earthquake probably broke the sealed parts of the fractures and dynamically increased the permeability[43]. Consequently, pore pressure migration caused the fluids to reach the swarm zone after 7 days. Seismological observations suggest that the pore pressure was as high as the minimum principal stress (lithostatic stress in this case) during the early stage of the swarm sequence[29]. Thus, our estimates of fluid volume and duration of fluid storage add more precise and detailed explanation for the scenario of swarm activity (Fig. 3a).

Assuming a geothermal gradient of 28–38 °C/km beneath the swarm region[38,44,45], the migration of estimated fluid volume induced SiO$_2$ precipitation[46] of 1.4×10^2–10^6 kg (see "Methods") that manifested as quartz veins, which are often observed in crustal rocks and deep-level ore deposit formations[47]. The majority of the ores (Au, Ag, Cu) in the arc crust precipitate at a temperature range of 450–100 °C[18]. The estimated fluid volume provides a key link between the geological observations (mineral veins and ore deposits) with periodic swarm activity. Contrary to the typical duration of ore formation in sub-million to a few million years[18], our observations suggest that smaller duration earthquake swarms (~2 years) can also produce detectable mineral veins and/or ore deposits.

The Yamagata-Fukushima swarm witnessed the release of crustal fluids that accumulated in the crust for 10^2–10^4 y. This study provides the first quantitative seismological evidence of fluid accumulation in the crust and its influence in causing earthquake swarm. The flux and periods of fluid accumulation obtained in this study, which covers the recurrence periods of M9 earthquakes, can be tested in future, whether the swarm recurrence time is consistent with the predicted fluid accumulation period. Further, we can discover the links between the swarm and M9 earthquakes by correlation between swarm recurrence and future M9 earthquakes. Furthermore, our approach provides a different perspective for understanding fluid-related phenomena in subduction zones and expands horizons for tracing the

spatiotemporal evolution of slab-derived fluids in the crust. Based on fluid volume, we provided a temporal linkage between the dynamic crustal seismicity and geological features, such as mineral precipitation. Further application in studying earthquake swarm sequences in other parts of volcanic arcs or other geological settings around the world will provide information on any heterogeneous behavior of slab-derived fluids, as well as its connection to the various fluid-related processes in subduction zones, such as episodic earthquakes, slow earthquakes, inland earthquakes, and volcanic activity.

Methods

Fluid volume estimation with injection-induced seismicity model McGarr's theory. McGarr[27] presented a theory to connect the injected fluid volume and the corresponding seismic moment released by elastic deformation. The relationship between the injected fluid volume and the cumulative seismic moment is described as:

$$\Sigma\mathrm{Mo} = \frac{2\mu(3\lambda + 2G)}{3}\triangle V, \qquad (1)$$

where Mo is the seismic moment, μ is the friction coefficient, λ and G are Lame's elastic parameters, and $\triangle V$ is the injected volume. Commonly, we assume $\lambda = G$ and $\mu = 0.6$. The simplified form of Eq. (1) is:

$$\Sigma\mathrm{Mo} = 2G\triangle V \qquad (2)$$

This model is widely used to estimate the maximum magnitude of induced seismicity associated with fluid injection in this form or other extended forms[28].

We inverted this relationship to estimate $\triangle V$ by inputting the cumulative observed seismic moments assuming G (modulus of rigidity) = 30 GPa[28]. As more detailed case, we also estimated $\lambda = 26.5$ GPa and $G = 3.3$ GPa with the method based on seismic velocity measurements of granite (see Darcy's law section) to fully utilize Eq. (1). It turns out to be $\Sigma\mathrm{Mo} = 58.43 \triangle V$, assuming $\mu = 0.6$, which is nearly equivalent to Eq. (1), with $G = 30$ GPa: $\Sigma\mathrm{Mo} = 60 \triangle V$. Considering our target depth, lithostatic pressure and pore pressure gradient (Supplementary Table 1), assuming a friction coefficient of 0.6 is also reasonable[48]. Even when we used $\mu = 0.85$, the estimates of fluid volume were 0.7 times smaller. The fluid volume estimate by McGarr's theory is currently 8.0×10^5 (Fig. 2) and can be reduced to 5.7×10^5 m^3. It does not make a big difference as estimates of both cases are in an order of 10^5.

Supplementary Fig. 2 show the time-series of the estimated fluid volume from the entire sequence and each cluster. The output of this model is sensitive to the magnitude of the events as its definition. Thus, a large amount of fluid was released during the first 50 days and was accompanied by intense seismic activity and moderate magnitude events.

This model provides the upper limit of the cumulative seismic moment when the entire injected volume converts the elastic energy into a seismic moment that is released without any energy loss, such as fluid leakage or conversion. Therefore, we should consider the estimated fluid volume from this method as the lower limit that caused the swarm sequence.

Seismogenic index. Shapiro[28] invented the seismogenic index (SI) model to assess the potential risk associated with fluid injection[49,50]. SI itself is a site-specific parameter representing the seismotectonic response to fluid injection. This model implicitly assumes that the induced seismicity value is related to the injected volume that migrates by diffusion. The SI model is defined as follows:

$$\Sigma = \log N_M(t) - \log V(t) + bM \qquad (3)$$

where Σ is the SI, N_M is the number of seismic events larger than M, M is the magnitude of the seismic event, V is the cumulative injected volume, and b is the b-value from the Gutenberg–Richter relationship. The SI becomes a function of the fluid volume and the Gutenberg–Richter parameter by introducing the Gutenberg–Richter law[51]: $\log N_M = a(t) - bM$.

$$= a(t) - \log V(t) \qquad (4)$$

We inverted this relationship to estimate the cumulative fluid volume, V. We estimated the a-values of the Gutenberg–Richter relationship from the swarm data using the maximum likelihood method[52] with Mc = 2.0, which was used in a previous study on this swarm sequence[29]. We chose the SI value range aiming to model the similar seismo-tectonic features. We referred to the previously observed SI values[28,30] from geothermal reservoirs in crystalline rock, where natural earthquake activity can be observed. We also considered the depth, rock type and b-value, then we set the upper bound to be 1.0, considering the Basel, Switzerland case ($\Sigma = 0.5$) and lower bound to be -2, considering the Soultz, France case ($\Sigma = -2.0$). We applied SI sets, from -2.0 to 1.0 with 0.5 increments, for fluid volume estimation and we regard SI = 0.5 (observed at Basel) as a representative case. A larger SI value denotes less fluid volume to explain the seismic sequence and vice versa.
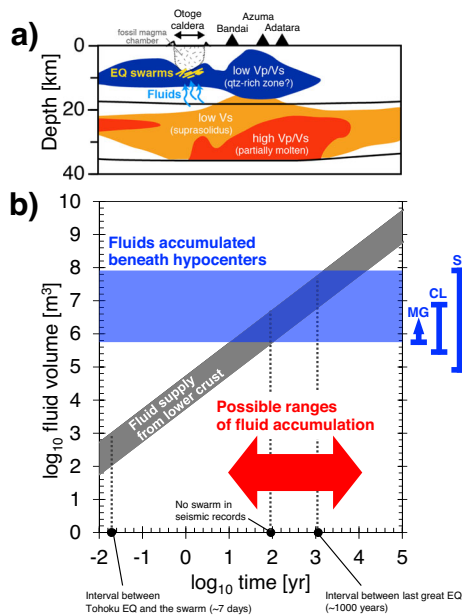
Fig. 3 Conceptual summarization of this study. a Schematic model of fluid supply below swarm regions. The seismic velocity structure[10] is interpreted based on ref. 38. The Miocene Otoge caldera is from ref. 36, the depths of the magma chambers of the Miocene fossil caldera in NE Japan are from refs. 21, 39. Earthquake (EQ) swarm is from ref. 14. **b** Estimation of periods of fluid accumulation. Fluid supply from the lower crust is based on refs. 8, 21, 39. Blue bars indicate the ranges of fluid volume estimated by each method. MG McGary's model, SI seismogenic index, CL cubic law, DL Darcy's law.

We computed the Gutenberg–Richter parameters in the time series by expanding the time window for each cluster. In Supplementary Figs. 3–5, the fluid volume estimation results with the SI model for the whole swarm sequence and each cluster are presented.

Fluid volume estimation with a hydrology model

Darcy's law. In addition to the injection-induced seismicity approaches, we directly modeled the spatiotemporal migration of a seismic swarm as a proxy of fluid flow using Darcy's law or the cubic law. Darcy's law is a well-accepted model in hydrology for describing fluid flow. In porous media, the hydraulic feature is characterized by the matrix permeability k [m²] and flow rate Q [m³/s] at cross-sectional area A [m²] invoked by the pressure difference ΔP [Pa] over the length of the flow path L [m] for the fluid with viscosity η [Pa·s], and can be described as follows:

$$Q = \frac{kA}{\eta L} \triangle P \qquad (5)$$

We assumed that the fluid flow that caused the swarm could be modeled using Darcy's law. We first estimated the diffusivity from the time-series hypocenter migration of the swarm based on Shapiro[31]. For each cluster and time step, the diffusivity is iteratively searched to fit 96% of the data (Supplementary Figs. 6–9). In Supplementary Figs. 6–9, we showed the example of time series evolution of seismic swarm front for each cluster. We checked the fits between the pressure front based on estimated diffusivity and observed seismic fronts. For cluster E and W (Supplementary Figs. 6 and 9), the pressure front did not describe the swarm event migration especially after 50 days. Very intense seismic activity in first 50 days after the Tohoku event presented very fast migration, so high diffusivity. Therefore, this caused the bias for the long-term diffusivity estimation as the algorithm tries to fit 96 % of whole events in the time window. For example, in Supplementary Fig. 6, time variable diffusivity surely covered most of the events, but triggering front lines did not fit the seismic front, even though time variable diffusivity decreased with time. So, to model the high (apparent) diffusivity at the early period of the swarm and to avoid overestimation of diffusivity later, we used two different ways to model diffusivity. For the first 50 days, we used the best fitted diffusivity and for the later period, we used the diffusivity of 0.2 m²/s, as shown in Supplementary Fig. 6. We visually checked the fit between the pressure front of 0.2 m²/s diffusivity and the data. For clusters N and S, we always used the best fitted diffusivity since we could confirm the reasonable fit on data.

Then, the diffusivity was converted to permeability, k, using Eq. (6) and the poroelastic modulus equation for crystalline rocks with low porosity (Eq. (7))[31].

$$D = Nk/\nu \qquad (6)$$

$$N = \left[\frac{\phi}{K_f} + \frac{\alpha}{K_g}\right]^{-1} \qquad (7)$$

where D is the diffusivity [m²/s], N is the poroelastic modulus, ν is the dynamic viscosity of the fluid, ϕ is the porosity, K_f is the fluid bulk modulus, $\alpha = 1 - K_d/K_g$, K_d is the dry-frame bulk modulus, and K_g is the grain material bulk modulus. Following Shapiro[31], we considered K_d as the bulk modulus of the rock body, then $K_d = 48.7$ GPa based on seismic velocity measurements of granite under high P–T conditions[53] that were modeled by ref. 54. We estimated $K_g = 58$ GPa for granite with a modal abundance of 20 vol.% quartz, 54 vol.% plagioclase, 23 vol.% K-feldspar, and 3 vol.% biotite at ~320 MPa and 375 °C[55]. We used $\phi = 0.62\%$ as the porosity of plutonic rocks under 250 MPa[56] and $K_f = 2.69$ GPa[57].

For viscosity (η), we used the value 1.24×10^{-4} Pa·s at 300 °C at 100 MPa[58] (hydrostatic conditions at 10 km). Finally, we assumed that this permeability was the apparent (matrix) permeability in the flow region. We explained the dimensions of the flow regions (A and L) and ΔP in the different sections.

Cubic law. The cubic law is a hydrological formulation similar to Darcy's law. When the fluid flow is assumed to occur in a single fracture, the flow rate in the fracture can be described using the cubic law Eq. (8). Instead of fracture permeability k, the fracture aperture d [m] is introduced to characterize the hydraulic features of the flow path.

$$Q = \frac{d^3}{12\eta} \frac{w}{L} \triangle P \qquad (8)$$

We can convert d to k using Eq. (9).

$$k = \frac{d^2}{12} \qquad (9)$$

We assumed that the fluid flow that caused the swarm could be modeled using the cubic law. We used 0.1 mm as fracture aperture[59], equivalent to a fracture permeability of ~8.0×10^{-10}. These values are consistent with the fracture permeability measured under experimental higher confining pressure conditions (100 MPa)[60].

When we calculated the flow rate Q, we assumed that channeling flow occurred at ~20% of the entire fault area[61], which was estimated from the hypocenter distribution. Therefore, we considered 20% of Q from Eq. (9) as the actual flow rate. From this analysis, we implicitly assumed that all fluid flows related to the swarm in multiple flow paths were modeled with fluid flow in one effective single fault.

Flow region. We detected the flow region from the time-variable hypocenter distribution of the swarm using 3D principal component analysis to extract the orientation and length of the cuboid flow region. Each of the three principal component orientations was compared with the time-series expansion of each cluster and was assigned a height, width, and length accordingly. The size of these cuboid dimensions was estimated as two factors of variance for each principal score, which means that 98% of the swarm events were included. We evaluated these parameters by expanding the time window for each cluster. The orientations and lengths of the three principal components are shown in Supplementary Figs. 10–14 for each cluster. Thus, A and L for Darcy's law, and w and L for the cubic law were estimated.

Pressure difference. We estimated the pressure difference in the driving force of the fluid flow from several observations. According to a previous study[29] that analyzed the focal mechanisms, many swarm events occurred from sub-horizontal faults at the early stage of the swarm sequence in the reverse fault stress regime. This observation suggests that the pore pressure should have increased as high as the lithostatic pressure at around 10 km depth. Therefore, we assumed that the pore pressure at the inlet of the flow region, which corresponds to the initial point of the seismic swarm, was equal to the lithostatic pressure of 270 MPa (27 MPa/km × 10 km), which means 170 MPa overpressure from hydrostatic conditions ($p_{hyd} = 100$ MPa). We also assumed that the pore pressure at the inlet linearly decreased with time and equalized with the pore pressure at the outlet, because the pore pressure should decrease due to fluid flow once the seal of the fault valve is broken.

We prepared several pore pressure difference scenarios at the flow region outlet (the edge of the swarm region), and set the range of outlet pore pressure from 0 to 260 MPa, which led to a pressure difference of 10–270 MPa. The most realistic case is that the outlet pressure is hydrostatic pressure that varies in the range of 70–100 MPa, according to the depth of the time-varying swarm region. In this case, the initial pressure difference is 170 MPa. As an extreme case, we assumed that the seismic region was dry (no water). In this situation, the outlet pressure is 0 MPa, which leads to a pore pressure difference of 270 MPa. Another realistic case is that the outlet pressure is the critical pore pressure for a well-oriented fault for a given stress field, assuming a friction coefficient of 0.6. Our previous study found that the

differential stress is approximately 20 MPa in this region[62]. We computed the critical pore pressure for a well-oriented fault to be 170.5 MPa, which is 100.5 MPa above the hydrostatic pressure at a depth of 7 km. This leads to a pore pressure difference of 69.5 MPa. We set the inlet pressure to linearly decrease with time and converge to the outlet pressure at 800 days. This is because the pore pressure source cannot maintain the initial pressure. Thus, we prepared various initial pressure difference cases, which provide a wide range of fluid volume estimation results using Darcy's law and the cubic law. However, we consider that the outlet pressure is hydrostatic pressure as the most realistic case (initial pressure difference 170 MPa).

Estimation of the amount of quartz precipitation during the fluid flow. The migration of large amounts of aqueous fluids from the deep crust to the shallower crust induces mass transfer that would be comparable to geological observations. Adopting a geothermal gradient of 28–38 °K/km beneath the swarm region[38,44,45], the solubility of SiO_2[46] at the base of the seismic swarm is 1600–4700 ppm (i.e., 12 km, 330–450 °C), which decreases to 70–180 ppm (i.e., 4 km, 100–150 °C), resulting in the precipitation of SiO_2 at 1.4×10^2–10^6 kg. This predicts the precipitation of large amounts of quartz, which would correspond to quartz veins that are often observed in crustal rocks and deep ore deposit formations[47]. The amount of precipitation may be even larger if the source of the fluids is deeper. The temperature range of 450–100 °C corresponds to the precipitation of major ore metals (Au, Ag, Cu) in the arc crust[18]. Indeed, although not a present mineralization, the Otoge caldera hosts Pliocene Au-Ag-Pb-Zn ore deposits formed at ~250–340 °C[63–65]. The present seismic activity under the Otoge caldera may trace a similar fluid pathway for past mineralization.

Data availability

Code availability

References

1. Hacker, B. R. H₂O subduction beyond arcs. *Geochem. Geophys. Geosyst.* **9**, Q03001 (2008).
2. Iwamori, H. Transportation of H₂O and melting in subduction zones. *Earth Planet. Sci. Lett.* **160**, 65–80 (1998).
3. Hasegawa, A., Nakajima, J., Umino, N. & Miura, S. Deep structure of the northeastern Japan arc and its implications for crustal deformation and shallow seismic activity. *Tectonophysics* **403**, 59–75 (2005).
4. Audet, P. & Bürgmann, R. Possible control of subduction zone slow-earthquake periodicity by silica enrichment. *Nature* **510**, 389–392 (2014).
5. Sibson, R. H., Robert, F. & Poulsen, K. H. High-angle reverse faults, fluid-pressure cycling, and mesothermal gold-quartz deposits. *Geology* **16**, 551–555 (1988).
6. Wannamaker, P. E. et al. Fluid and deformation regime of an advancing subduction system at Marlborough, New Zealand. *Nature* **460**, 733–736 (2009).
7. Van Keken, P. E., Hacker, B. R., Syracuse, E. M. & Abers, G. A. Subduction factory: 4. Depth-dependent flux of H₂O from subducting slabs worldwide. *J. Geophys. Res.* https://doi.org/10.1029/2010JB007922 (2011).
8. Kimura, J.-I. & Nakajima, J. Behaviour of subducted water and its role in magma genesis in the NE Japan arc: a combined geophysical and geochemical approach. *Geochim. Cosmochim. Acta* **143**, 165–188 (2014).
9. Ogawa, Y. et al. Magnetotelluric imaging of fluids in intraplate earthquake zones, NE Japan Back Arc. *Geophys. Res. Lett.* **28**, 3741–3744 (2001).
10. Nakajima, J., Matsuzawa, T., Hasegawa, A. & Zhao, D. Three-dimensional structure of Vp, Vs, and Vp/Vs beneath northeastern Japan: implications for arc magmatism and fluids. *J. Geophys. Res.* **106**, 21843–21857 (2001).
11. Sibson, R. H. Stress switching in subduction forearcs: Implications for overpressure containment and strength cycling on megathrusts. *Tectonophysics* **600**, 142–152 (2013).
12. Mindaleva, D. et al. Rapid fluid infiltration and permeability enhancement during middle–lower crustal fracturing: evidence from amphibolite–granulite-facies fluid–rock reaction zones, Sør Rondane Mountains, East Antarctica. *Lithos* **372–373**, 105521 (2020).
13. Nakajima, J. & Uchida, N. Repeated drainage from megathrusts during episodic slow slip. *Nat. Geosci.* **11**, 351–356 (2018).
14. Yoshida, K. & Hasegawa, A. Hypocenter migration and seismicity pattern change in the Yamagata-Fukushima border, NE Japan, caused by fluid movement and pore pressure variation. *J. Geophys. Res. Solid Earth* **123**, 5000–5017 (2018).
15. Okada, T. et al. Hypocenter migration and crustal seismic velocity distribution observed for the inland earthquake swarms induced by the 2011 Tohoku-Oki earthquake in NE Japan: implications for crustal fluid distribution and crustal permeability. *Geofluids* **15**, 293–309 (2015).
16. Kisslinger, C. Processes during the Matsushiro, Japan, earthquake swarm as revealed by leveling, gravity, and spring-flow observations. *Geology* **3**, 57–62 (1975).
17. Micklethwaite, S. & Cox, S. F. Progressive fault triggering and fluid flow in aftershock domains: Examples from mineralized Archaean fault systems. *Earth Planet. Sci. Lett.* **250**, 318–330 (2006).
18. Sillitoe, R. H. Porphyry copper systems. *Econ. Geol.* **105**, 3–41 (2010).
19. Agroli, G., Okamoto, A., Uno, M. & Tsuchiya, N. Transport and evolution of supercritical fluids during the formation of the Erdenet Cu–mo Deposit, Mongolia. *Geosciences* **10**, 201 (2020).
20. Cox, S. F. Injection-driven swarm seismicity and permeability enhancement: implications for the dynamics of hydrothermal ore systems in high fluid-flux, overpressured faulting regimes—an invited paper. *Econ. Geol.* **111**, 559–587 (2016).
21. Amanda, F. F., Yamada, R., Uno, M., Okumura, S. & Tsuchiya, N. Evaluation of caldera hosted geothermal potential during volcanism and magmatism in subduction system, NE Japan. *Geofluids* **2019**, 1–14 (2019). 3031586.
22. Uno, M., Okamoto, A. & Tsuchiya, N. Excess water generation during reaction-inducing intrusion of granitic melts into ultramafic rocks at crustal P–T conditions in the Sør Rondane Mountains of East Antarctica. *Lithos* **284–285**, 625–641 (2017).
23. Freundt, A. et al. Volatile (H₂O, CO₂, Cl, S) budget of the Central American subduction zone. *Int. J. Earth Sci.* **103**, 2101–2127 (2014).
24. Tsuchiya, N., Yamada, R. & Uno, M. Supercritical geothermal reservoir revealed by a granite–porphyry system. *Geothermics* **63**, 182–194 (2016).
25. Yoshida, K. & Hasegawa, A. Sendai-Okura earthquake swarm induced by the 2011 Tohoku-Oki earthquake in the stress shadow of NE Japan: detailed fault structure and hypocenter migration. *Tectonophysics* **733**, 132–147 (2018).
26. Shelly, D. R., Ellsworth, W. L. & Hill, D. P. Fluid-faulting evolution in high definition: Connecting fault structure and frequency-magnitude variations during the 2014 Long Valley Caldera, California, earthquake swarm. *J. Geophys. Res. Solid Earth* **121**, 1776–1795 (2016).
27. McGarr, A. Maximum magnitude earthquakes induced by fluid injection. *J. Geophys. Res. Solid Earth* **119**, 1008–1019 (2014).
28. Shapiro, S. A., Dinske, C., Langenbruch, C. & Wenzel, F. Seismogenic index and magnitude probability of earthquakes induced during reservoir fluid stimulations. *Leading Edge* **29**, 304–309 (2010).
29. Yoshida, K., Saito, T., Urata, Y., Asano, Y. & Hasegawa, A. Temporal changes in stress drop, frictional strength, and earthquake size distribution in the 2011 Yamagata-Fukushima, NE Japan, earthquake swarm, caused by fluid migration. *J. Geophys. Res. Solid Earth* **122**, 10,379–10,397 (2017).
30. Dinske, C. & Shapiro, S. A. Seismotectonic state of reservoirs inferred from magnitude distributions of fluid-induced seismicity. *J. Seismol.* **17**, 13–25 (2013).
31. Shapiro, S. A., Huenges, E. & Borm, G. Estimating the crust permeability from fluid-injection-induced seismic emission at the KTB site. *Geophys. J. Int.* **131**, F15–F18 (1997).
32. Hiraga, T., Nagase, T. & Akizuki, M. The structure of grain boundaries in granite-origin ultramylonite studied by high-resolution electron microscopy. *Phys. Chem. Min.* **26**, 617–623 (1999).
33. Secor, D. T. Jr & Pollard, D. D. On the stability of open hydraulic fractures in the Earth's crust. *Geophys. Res. Lett.* **2**, 510–513 (1975).
34. Takei, Y. Effect of pore geometry on VP/VS: from equilibrium geometry to crack. *J. Geophys. Res.* https://doi.org/10.1029/2001JB000522 (2002).
35. Tamura, Y., Tatsumi, Y., Zhao, D., Kido, Y. & Shukuno, H. Hot fingers in the mantle wedge: New insights into magma genesis in subduction zones. *Earth Planet. Sci. Lett.* **197**, 105–116 (2002).
36. Yoshida, T. et al. Late Cenozoic igneous activity and crustal structure in the NE Japan arc: background of inland earthquake activity. *J. Geogr.* **129**, 529–563 (2020).
37. Matsubara, M., Hirata, N., Sato, H. & Sakai, S. Lower crustal fluid distribution in the northeastern Japan arc revealed by high-resolution 3D seismic tomography. *Tectonophysics* **388**, 33–45 (2004).
38. Nishimoto, S., Ishikawa, M., Arima, M., Yoshida, T. & Nakajima, J. Simultaneous high P-T measurements of ultrasonic compressional and shear wave velocities in Ichino-megata mafic xenoliths: their bearings on seismic

velocity perturbations in lower crust of northeast Japan arc. *J. Geophys. Res.* **113**, 1–18 (2008).

39. Suzuki, T., Uno, M., Okumura, S., Yamada, R. & Tsuchiya, N. Differentiation of eruptive magma in the Late Miocene Shirasawa Caldera and present geothermal reservoir. *J. Geotherm. Res. Soc. Jpn* **39**, 25–37 (2017).

40. Ushioda, M., Takahashi, E., Hamada, M. & Suzuki, T. Water content in arc basaltic magma in the Northeast Japan and Izu arcs: an estimate from Ca/Na partitioning between plagioclase and melt. *Earth Planet Space* **66**, 1–10 (2014).

41. Umino, N., Ujikawa, H., Hori, S. & Hasegawa, A. Distinct S-wave reflectors (bright spots) detected beneath the Nagamachi-Rifu fault, NE Japan. *Earth Planet Space* **54**, 1021–1026 (2014).

42. Hori, S., Umino, N., Kono, T. & Hasegawa, A. Distinct S-wave reflectors (bright spots) extensively distributed in the crust and upper mantle beneath the Northeastern Japan arc. *J. Seismol. Soc. Jpn* **56**, 435–446 (2004).

43. Brodsky, E. E. & Kanamori, H. Elastohydrodynamic lubrication of faults. *J. Geophys. Res.* **106**, 16357–16374 (2001).

44. Muto, J. Rheological structure of northeastern Japan lithosphere based on geophysical observations and rock mechanics. *Tectonophysics* **503**, 201–206 (2011).

45. Tanaka, A. Geothermal gradient and heat flow data in and around Japan (II). Crustal thermal structure and its relationship to seismogenic layer. *Earth Planet Space* **56**, 1195–1199 (2014).

46. Manning, C. E. The solubility of quartz in H_2O in the lower crust and upper mantle. *Geochim. Cosmochim. Acta* **58**, 4831–4839 (1994).

47. Weatherley, D. K. & Henley, R. W. Flash vaporization during earthquakes evidenced by gold deposits. *Nat. Geosci.* **6**, 294–298 (2013).

48. Byerlee, J. Friction of rocks. *Pageoph* **116**, 615–626 (1978).

49. Langenbruch, C. & Zoback, M. D. How will induced seismicity in Oklahoma respond to decreased saltwater injection rates? *Sci. Adv.* **2**, 1601542 (2016).

50. Schultz, R., Atkinson, G., Eaton, D. W., Gu, Y. J. & Kao, H. Hydraulic fracturing volume is associated with induced earthquake productivity in the duvernay play. *Science* **359**, 304–308 (2018).

51. Gutenberg, B. & Richter, C. F. Frequency of earthquakes in California. *Bull. Seismol. Soc. Am.* **34**, 185–188 (1944).

52. Wiemer, S. A software package to analyze seismicity: ZMAP. *Seismol. Res. Lett.* **72**, 373–382 (2001).

53. Kern, H., Gao, S., Jin, Z., Popp, T. & Jin, S. Petrophysical studies on rocks from the Dabie ultrahigh-pressure (UHP) metamorphic belt, Central China: implications for the composition and delamination of the lower crust. *Tectonophysics* **301**, 191–215 (1999).

54. Iwamori, H. et al. Simultaneous analysis of seismic velocity and electrical conductivity in the crust and the uppermost mantle: a forward model and inversion test based on grid search. *J. Geophys. Res. Solid Earth* **126**, 2021JB022307 (2021).

55. Hacker, B. R. & Abers, G. A. Subduction factory 3: an Excel worksheet and macro for calculating the densities, seismic wave speeds, and H_2O contents of minerals and rocks at pressure and temperature. *Geochem. Geophys. Geosyst.* **5**, 1–7 (2004).

56. Watanabe, T. & Higuchi, A. Simultaneous measurements of elastic wave velocities and electrical conductivity in a brine-saturated granitic rock under confining pressures and their implication for interpretation of geophysical observations. *Prog. Earth Planet. Sci.* **2**, 37 (2015).

57. Wagner, W. & Pruss, A. Revised release on the {IAPWS} formulation 1995 for the thermodynamic properties of ordinary water substance for general and scientific use. *J. Phys. Chem. Ref. Data* **31**, 387–535 (2002).

58. Huber, M. L. et al. New international formulation for the viscosity of H_2O. *J. Phys. Chem. Ref. Data* **38**, 101–125 (2009).

59. Norbeck, J. H. & Shelly, D. R. Exploring the role of mixed-mechanism fracturing and fluid-faulting interactions during the 2014 Long Valley Caldera, California, Earthquake Swarm. In *Proc. 43rd Workshop on Geothermal Reservoir Engineering* 1–16 (Stanford University, 2018).

60. Watanabe, N., Hirano, N. & Tsuchiya, N. Diversity of channeling flow in heterogeneous aperture distribution inferred from integrated experimental-numerical analysis on flow through shear fracture in granite. *J. Geophys. Res. Solid Earth* **114**, 1–17 (2009).

61. Ishibashi, T., Watanabe, N., Hirano, N., Okamoto, A. & Tsuchiya, N. Beyond-laboratory-scale prediction for channeling flows through subsurface rock fractures with heterogeneous aperture distributions revealed by laboratory evaluation. *J. Geophys. Res. Solid Earth* **120**, 106–124 (2015).

62. Yoshida, K., Hasegawa, A. & Yoshida, T. Temporal variation of frictional strength in an earthquake swarm in NE Japan caused by fluid migration. *J. Geophys. Res. Solid Earth* **121**, 5953–5965 (2016).

63. Zeng, N., Izawa, E., Watanabe, K. & Itaya, T. Timing of Au-Ag mineralization and related volcanism at Otoge, Yamagata Prefecture, Northeast Japan. *J. Mineral. Petrol. Econ. Geol.* **91**, 297–304 (1996).

64. Watanabe, M., Hoshino, K., Myint, K., Miyazaki, K. & Nishido, H. Stannite from the Otoge kaolin-pyrophyllite deposits, Yamagata prefecture, NE Japan and its genetical significance. *Resour. Geol.* **44**, 439–444 (1994).

65. Shikazono, N. K-Ar ages for the Yatani Pb-Zn-Au-Ag vein-type deposits and Otoge kaolin-pyrophyllite, Yamagata prefecture, northeastern part of Japan. *Min. Geol.* **35**, 205–209 (1985).

66. Wessel, P. & Smith, W. H. F. New, improved version of the Generic Mapping Tools released. *Eos. Trans. AGU* **79**, 579 (1998).

Author contributions

Y.M., M.U., and K.Y. designed the study. K.Y. preprocessed the earthquake swarm data. Y.M. and M.U. performed the fluid volume estimation analysis. M.U. performed the geological analyses. All authors have discussed and interpreted the results and wrote the manuscript.

Competing interests

The authors declare no competing interests.

Additional information

Supplementary information The online version contains supplementary material available at https://doi.org/10.1038/s43247-022-00610-7.

Correspondence and requests for materials should be addressed to Yusuke Mukuhira.

Peer review information *Communications Earth & Environment* thanks Wasja Bloch and the other anonymous reviewer(s) for their contribution to the peer review of this work. Primary handling editors: Luca Dal Zilio, Joe Aslin. Peer reviewer reports are available.

Reprints and permission information is available at http://www.nature.com/reprints

Publisher's note Springer Nature remains neutral with regard to jurisdictional claims in published maps and institutional affiliations.